



HAL
open science

Single-nanotube tracking reveals the nanoscale organization of the extracellular space in the live brain

Antoine G. Godin, Juan A. Varela, Zhenghong Gao, Noémie Danné, Julien P. Dupuis, Brahim Lounis, Laurent Groc, Laurent Cognet

► To cite this version:

Antoine G. Godin, Juan A. Varela, Zhenghong Gao, Noémie Danné, Julien P. Dupuis, et al.. Single-nanotube tracking reveals the nanoscale organization of the extracellular space in the live brain. Nature Nanotechnology, 2016, 12 (3), pp.238 - 243. 10.1038/NNANO.2016.248 . hal-01630795

HAL Id: hal-01630795

<https://hal.science/hal-01630795v1>

Submitted on 13 Nov 2017

HAL is a multi-disciplinary open access archive for the deposit and dissemination of scientific research documents, whether they are published or not. The documents may come from teaching and research institutions in France or abroad, or from public or private research centers.

L'archive ouverte pluridisciplinaire **HAL**, est destinée au dépôt et à la diffusion de documents scientifiques de niveau recherche, publiés ou non, émanant des établissements d'enseignement et de recherche français ou étrangers, des laboratoires publics ou privés.

1 **Title : Single nanotube tracking reveals the**
2 **extracellular space nanoscale organization in live**
3 **brain tissue**

4 Antoine G. Godin^{1,2,*}, Juan A. Varela^{3,4,*}, Zhenghong Gao^{1,2,*}, Noémie Dannée^{1,2},
5 Julien P. Dupuis^{3,4}, Brahim Lounis^{1,2}, Laurent Groc^{3,4} and Laurent Cognet^{1,2}

6 **Affiliations**

7 ¹Univ. Bordeaux, Laboratoire Photonique Numérique et Nanosciences, UMR 5298, F-33400
8 Talence, France

9 ²Institut d'Optique & CNRS, LP2N UMR 5298, F-33400 Talence, France

10 ³Univ. Bordeaux, Interdisciplinary Institute for Neuroscience, UMR 5297, F-33000 Bordeaux,
11 France

12 ⁴CNRS, IINS UMR 5297, F-33000 Bordeaux, France

13 *These authors contributed equally to this work.

14 **The brain is a dynamic structure in which the extracellular space (ECS) takes up**
15 **almost a quarter of its volume¹⁻². Signalling molecules, neurotransmitters and nutrients**
16 **transit *via* the ECS which constitutes a key microenvironment for cellular communication³**
17 **and clearance of toxic metabolites. The ECS spatial organization varies during sleep⁴,**
18 **development⁵, aging⁶ and is likely altered in neuropsychiatric and degenerative diseases⁷,**
19 **as inferred from electron microscopy⁸⁻⁹ and macroscopic biophysical investigations^{2,10}.**
20 **Here we show an approach to directly observe the local ECS structures and rheology in a**
21 **brain tissue using super-resolution imaging. We inject single-walled carbon nanotubes**
22 **(SWCNTs) in rat cerebroventricles and follow individual nanotubes near-IR emission for**
23 **tens of minutes in acute slices as they diffuse inside the ECS. Because of the interplay**
24 **between the nanotube geometry and the ECS local environment, we can extract**
25 **information about the ECS dimension and local viscosity. We find a striking diversity of**
26 **ECS dimensions down to 40 nm, and as well as of local viscosity values. Moreover, by**

27 **chemically altering the brain extracellular matrix of the live animals before nanotube**
28 **injection, we reveal that ECS rheology properties are affected, but that ECS alterations are**
29 **local and inhomogeneous at nanoscale dimensions.**

30 Investigations of the fine structure of live brain ECS require brain preparations that best
31 preserve cellular architectures. In that respect, we used acute brain slices as opposed to other
32 preparations that poorly preserve native tissue organization, e.g. cultured neurons or organotypic
33 slices. Moreover, one needs an imaging modality reaching spatial resolutions beyond the
34 diffraction limit as well as tissue access deeper than the first 2-3 pyramidal cell layers inside the
35 slice ($> \sim 30\mu\text{m}$) to avoid regions affected during slicing. To this aim, deep tissue localization
36 microscopy based on tracking the successive positions of single nano-emitters while they explore
37 brain tissues would represent a unique approach.

38 Near-infrared luminescent SWCNTs were previously proposed as unique probes for ensemble
39 imaging in whole animal¹¹⁻¹² due to their brightness, photostability and spectral imaging range¹³⁻
40 ¹⁴, as well as for intracellular single molecule tracking in cultured cells¹⁵⁻¹⁶. It was also shown, at
41 the ensemble level, that their unusual length-to-diameter aspect ratios contribute to enhance their
42 penetration within multicellular tumour spheroids depending on the encapsulation agents used¹⁷⁻
43 ¹⁸. In fact, in contrast to spherical nanoparticles, SWCNTs have two characteristic dimensions
44 impacting their diffusion behaviours. Their small diameter (nanometer scale) confers them a
45 remarkable accessibility in complex environments, while the combination of their length and
46 rigidity can moderate their diffusion rates so as to be compatible with video-rate single molecule
47 imaging¹⁹.

48 SWCNTs were delivered into young rat brains by injection of a small volume (5 μl ,
49 3 $\mu\text{g}/\text{mL}$) of solubilized nanotubes in the lateral cerebroventricles (Figure 1a)²⁰. This SWCNT
50 delivery method generates minimal tissue inflammation as the gross morphology and density of
51 microglial cells – the resident macrophages of the brain- were found to be similar in buffer- and
52 SWCNT-injected brains (Figure S1). SWCNTs coated with phospholipid-polyethylene glycol
53 (PL-PEG) were used since they display low cytotoxicity as compared to other encapsulation
54 methods of luminescent SWCNTs²¹⁻²². Rats were sacrificed 30 min after the ventricular injection
55 and acute brain slices were prepared for observation under a wide field fluorescent NIR
56 microscope (Figure 1b). Wavelengths of excitation (845 nm to excite (6,5) SWCNTs at a phonon

57 sideband²³) and emission (986 nm for (6,5) SWCNTs) are in the transparency window of the
58 studied brain tissues (Figure 1c) and as such, minimize tissue phototoxicity (Figures S2 and S3).
59 Phonon sideband excitation also ensures better emission photostability²³ as compared to high
60 photon-energy excitation commonly used to excite SWCNT at their second order electronic
61 transition (Figure S4).

62 Single luminescent (6,5) SWCNTs were detected in diverse areas of sagittal brain slices
63 (e.g. neocortex, hippocampus, striatum) (Figure S5). Imaging was performed at different depths
64 in the brain slices, from a few tens of μm to avoid the damaged superficial layers up to $\sim 100 \mu\text{m}$
65 (Figure S6). The broad SWCNT dissemination away from cerebroventricular injection site was
66 surely facilitated by their nanometer-size diameters, and also suggests that SWCNTs were
67 primarily located in the ECS since such a large dissemination would not be possible if SWCNTs
68 were internalized in brain cells. The diffusion of molecules in the ECS is thought to be globally
69 governed by several parameters such as the geometric path length, trapping in dead space
70 domains, and ECS viscosity by molecular crowding and transient molecular interactions. At a
71 macroscopic scale, these parameters participate to the so-called tortuosity of the ECS^{2,24}. Many
72 SWCNTs were found immobilized away from the ventricular injection zones, likely originating
73 from non-specific interactions with molecules of the ECS (although PL-PEG coating minimizes
74 this effect in live cell culture (Figure S7) and live animals²¹), and/or by the existence of dead-
75 space microdomains². The direct observation of PL-PEG-coated SWCNT trapping is thus
76 consistent with the existence dead-space domains in the ECS. To further ascertain extracellular
77 location, we directly loaded SWCNTs within hippocampal pyramidal neurons through a patch-
78 clamp pipette. The behaviours of detected intracellular SWCNTs were distinct from
79 cerebroventricular injected ones (Figure S8), further supporting that SWCNTs imaged after icv
80 injection are primarily extracellular.

81 The movements of individual SWCNTs exploring the ECS could be resolved with video
82 rate fluorescence imaging (Figure 1d). This is primarily due to the SWCNT high aspect-ratio and
83 rigidity, linked to their nanometer diameter, which significantly slows down their diffusion in the
84 ECS maze, as compared to nanometer sized probes or fully flexible polymers. We indeed
85 checked that small isotropic fluorescent probes diffuse too fast in the ECS to be imaged at video
86 rate for a long time (observed trajectories $< 1\text{s}$, Figure S9). In addition, we could record long
87 movies of single SWCNT (x, y) diffusion occurring during more than 20,000 frames within the

88 $\sim 1\mu\text{m}$ depth-of-focus of the microscope (Movie 1). By means of two-dimensional asymmetric
 89 Gaussian fitting analysis, we extracted in each movie frame i the nanotube center-of-mass
 90 localization (x_i, y_i) in the imaging plane with sub-wavelength precision (~ 40 nm) and its axis
 91 orientation θ_i relative to the x axis in the laboratory frame (Figure 1c, inset). Analysis of the
 92 fitted 2D Gaussian asymmetry provides a measure of the nanotube lengths L which range here
 93 from ~ 490 - 780 nm. These lengths match the typical SWCNT lengths of the injected solution
 94 determined by AFM imaging (Figure S10). Assuming characteristic ECS dimensions ξ larger
 95 than 50 nm, these SWCNTs behave as rigid rods in the ECS and their diffusion should be
 96 independent of flexibility¹⁹. The nanotube movements along (\parallel) and perpendicular (\perp) to their
 97 axis were then decoupled to calculate two 1D Mean Squared Displacements MSD_{\parallel} and MSD_{\perp} as
 98 a function of time (Figure 2a). The MSD_{xy} corresponding to the 2D movements in the laboratory
 99 frame was also calculated. On short time scales ($t < t_c \sim 200$ ms), MSD_{xy} is linear with time
 100 and $MSD_{xy} \sim MSD_{\parallel} + MSD_{\perp}$ while for longer times MSD_{xy} levels off and $MSD_{\parallel} + MSD_{\perp}$ is
 101 close to linear, such that $MSD_{xy} < MSD_{\parallel} + MSD_{\perp}$ (Figure 2a). The different behaviours of
 102 MSD_{xy} and $MSD_{\parallel} + MSD_{\perp}$ indicates that nanotube movements are not free²⁵ and thus
 103 constrained by local ECS environment. The deviation from linearity of MSD_{xy} also suggests that
 104 t_c represents a characteristic time scale during which SWCNTs explore single ECS sub-domains.

105 Because $MSDs$ calculated on full trajectories inherently reflect average displacements,
 106 the properties of transient diffusive states can hardly be retrieved by the direct analysis of
 107 MSD_{xy} , MSD_{\parallel} or MSD_{\perp} . To access transient diffusive states in local environments, we used
 108 instead an analytical analysis based on the Distribution of Squared Displacements (DSD)²⁶⁻²⁷
 109 along and perpendicular to the nanotube axis $DSD_{\tau}(r_{\parallel,\perp}^2)$ defined for different time
 110 lags τ with $\tau < t_c$ (supplemental materials). Along each direction (\parallel, \perp), two diffusion
 111 behaviors are found characterized by the time dependence of their mean $MSDs$ denoted
 112 $\langle r_{\parallel,\perp}^2 \rangle_j(\tau)$, where $j = 1$ corresponds to the slowest SWCNT diffusive states and $j = 2$ to faster
 113 ones (Figure S11). The population of small displacements perpendicular to SWCNT axis is
 114 bounded as evidenced by the fast saturation of $\langle r_{\perp}^2 \rangle_1(\tau)$ (Figure 2b) while other states display
 115 mainly unrestricted diffusion (Figure 2b and S11). This behaviour can be related to successive
 116 diffusion episodes occurring in different ECS confinement domains (see below). The plateau of
 117 $\langle r_{\perp}^2 \rangle_1(\tau)$, which equals $\langle \xi \rangle^2 / 6$ for confined diffusion along a 1D coordinate²⁸, provides a

118 measure of $\langle \xi \rangle$ representing the average confining ECS dimension (Figure 2b). As displayed in
119 Figure 2c, $\langle \xi \rangle$ ranges from 80 to 270 nm (150 ± 40 nm, mean \pm SD). This dynamic analysis
120 demonstrates that anisotropic diffusion behaviours of single SWCNTs locally probe the brain
121 ECS and can reveal nanoscale dimensions (Figure 2d).

122 Using a similar approach as in single-molecule localization microscopy²⁹, a large number
123 of nanotube localization coordinates obtained with sub-diffraction precisions were pooled to
124 create a super-resolved image of the ECS (Figure 3a). Such images directly unveil the spatial,
125 nanoscale and structural tortuosity of the live brain ECS. The ECS maze is heterogeneous and
126 consists of many connected submicron structural domains of various sizes. A total of 419 ECS
127 domains were identified with typical dimensions ξ ranging from ~ 50 to 700 nm (Figure 3b and
128 S12). Noteworthy, the ECS nanoscale dimensions and morphologies described here in live brain
129 samples resembles the ECS morphology visualized by electron microscopy following cryo-
130 fixation of brain tissues⁸⁻⁹ (Figure S13). Maps of the instantaneous diffusion constants calculated
131 along nanotube trajectories on 300 ms sliding time windows were constructed (Figure 3c) to
132 evaluate the spatial dependence of the local SWCNT diffusion in live brain tissue. From the
133 knowledge of nanotube lengths, high-resolution spatial maps of the ECS viscosity were also
134 obtained (Figure 3c and Extended Data Movie 1). Viscosity values ranged from ~ 1 to 50 mPa·s
135 which is up to two orders of magnitude larger than that of the cerebrospinal fluid. These
136 viscosity maps reveal that ECS local viscosity is spatially inhomogeneous. Interestingly, within
137 this viscosity range, the instantaneous diffusion constants of quantum dots in the ECS, having
138 hydrodynamic diameters of 35 nm would locally vary from ~ 0.1 to $10 \mu\text{m}^2\text{s}^{-1}$. As expected,
139 the average diffusion constant of such quantum dots ($\sim 0.1 \mu\text{m}^2\text{s}^{-1}$) previously observed on
140 macroscopic spatial scales in the ECS²⁴ is constrained towards the smallest local values and
141 cannot divulge the diversity of local viscosities. By comparing Figures 3a&c, the spatial
142 dependence of the ECS rheological properties indicates that locally ECS viscosity values do not
143 correlate with ECS dimensions. Indeed, although ξ values span up to two orders of magnitude,
144 SWCNT instantaneous diffusion constants vary over up to three decades independently of the
145 ECS dimensions in which SWCNTs are diffusing. Although bearing diffusion properties not
146 necessarily identical to those of endogenous molecules diffusing in the brain ECS, our findings
147 demonstrate that SWCNT tracking unveils and quantifies the diversity of nanoscale diffusive
148 environments composing the ECS. Interestingly, considering the ECS as a fluidic connected

149 space with specialized functional regions^{2,4}, our results indicate that local structural dimensions
150 are not sole responsible for affecting molecular diffusion properties of the ECS. It follows that
151 other mechanisms including fine-tuned molecular interactions involving constitutive components
152 of the ECS must play an important role for controlling local diffusion of e.g. endogenous
153 signalling molecules or nutrients in local areas of interest.

154 In order to support this hypothesis, we then biochemically altered the ECS structure by
155 injecting hyaluronidase in the brain lateral ventricles of young rats several hours before nanotube
156 injection and imaging, a time period supposedly sufficient to significantly digest hyaluronic
157 acid³⁰. We first confirmed alterations of the ECM components in hyaluronidase-injected brains
158 as attested by strong decrease of both hyaluronan binding protein (HABP) (Figures 4a-d) and
159 aggrecan immunostaining (Extended Figure 14). Noteworthy, we did not observe modification of
160 the morphology of neuronal soma and overall cellular density in hyaluronidase-injected brains at
161 spinning-disk confocal resolution. Analysis of SWCNT diffusion indicates that they explored
162 wider areas as compared to naive brains within identical time scales (Figures 4e&f). Consistent
163 with hyaluronidase-induced disappearance of ECM components, instantaneous diffusion
164 coefficients were significantly increased (calculated as in Figure 3b), indicating a global
165 reduction of medium viscosity (Figures 4g&h, Movie 2). More precisely, the histogram of
166 diffusion coefficients from naive brains was well fitted by a single lognormal distribution
167 whereas in the altered brains two lognormal distributions were needed, with one of them being
168 indistinguishable from the one used to fit the histogram of naive brains (Figure 4h). This
169 demonstrates that hyaluronidase effect is in fact not spatially homogeneous in the ECS (see also
170 Figure 4g). Characterizing the ECS dimensions explored by SWCNTs using the DSD analysis, a
171 moderate but significant reduction of mean size values $\langle \xi \rangle$ was found in altered brain
172 (280 ± 60 nm) as compared to naive ones (150 ± 40 nm) (Figure 4i). This indicates that upon
173 profound but non-uniform alteration of the ECM, the ECS topology offers larger territories for
174 SWCNT nanoscale molecular exploration.

175 Here, we provide a new approach to reveal the ECS dimensions and viscosity at the
176 nanoscale in live brain tissue of young rats. The ECS appears as a maze of interconnected
177 polymorphic compartments structured down to the nanoscale and bearing specific rheological
178 properties. This knowledge will surely influence our understanding of the chemical-based

179 cellular communication in brain physiology and pathology. In addition, detailed knowledge of
180 nanoscale ECS network should also foster new drug delivery strategies.

181

182 **References**

- 183 1 Cserr, H. F. *et al.* Extracellular volume decreases while cell-volume is maintained by ion uptake in rat-
184 brain during acute hypernatremia. *J. Physiol.-London* **442**, 277-295 (1991).
- 185 2 Sykova, E. & Nicholson, C. Diffusion in brain extracellular space. *Physiol. Rev.* **88**, 1277-1340 (2008).
- 186 3 Dityatev, A., Schachner, M. & Sonderegger, P. The dual role of the extracellular matrix in synaptic
187 plasticity and homeostasis. *Nat. Rev. Neurosci.* **11**, 735-746 (2010).
- 188 4 Xie, L. *et al.* Sleep drives metabolite clearance from the adult brain. *Science* **342**, 373-377 (2013).
- 189 5 Lehmenkuhler, A., Sykova, E., Svoboda, J., Zilles, K. & Nicholson, C. Extracellular space parameters in
190 the rat neocortex and subcortical white matter during postnatal development determined by diffusion
191 analysis. *Neuroscience* **55**, 339-351 (1993).
- 192 6 Metzler-Baddeley, C., Jones, D. K., Belaroussi, B., Aggleton, J. P. & O'Sullivan, M. J. Frontotemporal
193 connections in episodic memory and aging: a diffusion MRI tractography study. *J. Neurosci.* **31**, 13236-
194 13245 (2011).
- 195 7 Berezin, V., Walmod, P. S., Filippov, M. & Dityatev, A. Targeting of ECM molecules and their
196 metabolizing enzymes and receptors for the treatment of CNS diseases. *Prog. Brain Res.* **214**, 353-388
197 (2014).
- 198 8 Ohno, N., Terada, N., Saitoh, S. & Ohno, S. Extracellular space in mouse cerebellar cortex revealed by in
199 vivo cryotechnique. *J. Comp. Neurol.* **505**, 292-301 (2007).
- 200 9 Korogod, N., Petersen, C. C. & Knott, G. W. Ultrastructural analysis of adult mouse neocortex comparing
201 aldehyde perfusion with cryo fixation. *Elife* **4** (2015).
- 202 10 Verkman, A. S. Diffusion in the extracellular space in brain and tumors. *Phys. Biol.* **10**, 045003 (2013).
- 203 11 Welsher, K. *et al.* A route to brightly fluorescent carbon nanotubes for near-infrared imaging in mice. *Nat.*
204 *Nanotechnol.* **4**, 773-780 (2009).
- 205 12 Heller, D. A. *et al.* Multimodal optical sensing and analyte specificity using single-walled carbon
206 nanotubes. *Nat. Nanotechnol.* **4**, 114-120 (2009).
- 207 13 Bachilo, S. M. *et al.* Structure-assigned optical spectra of single-walled carbon nanotubes. *Science* **298**,
208 2361-2366 (2002).
- 209 14 Cognet, L. *et al.* Stepwise quenching of exciton fluorescence in carbon nanotubes by single-molecule
210 reactions. *Science* **316**, 1465-1468 (2007).
- 211 15 Reuel, N. F., Dupont, A., Thouvenin, O., Lamb, D. C. & Strano, M. S. Three-dimensional tracking of
212 carbon nanotubes within living cells. *ACS Nano* **6**, 5420-5428 (2012).
- 213 16 Fakhri, N. *et al.* High-resolution mapping of intracellular fluctuations using carbon nanotubes. *Science* **344**,
214 1031-1035 (2014).
- 215 17 Wang, Y., Bahng, J. H., Che, Q., Han, J. & Kotov, N. A. Anomalously Fast Diffusion of Targeted Carbon
216 Nanotubes in Cellular Spheroids. *ACS Nano* **9**, 8231-8238 (2015).
- 217 18 Jena, P. V. *et al.* Photoluminescent carbon nanotubes interrogate the permeability of multicellular tumor
218 spheroids. *Carbon NY* **97**, 99-109 (2016).
- 219 19 Fakhri, N., MacKintosh, F. C., Lounis, B., Cognet, L. & Pasquali, M. Brownian motion of stiff filaments in
220 a crowded environment. *Science* **330**, 1804-1807 (2010).

221 20 Varela, J. A. *et al.* Targeting neurotransmitter receptors with nanoparticles in vivo allows single-molecule
222 tracking in acute brain slices. *Nat Commun* **7**, 10947 (2016).

223 21 Liu, Z. *et al.* In vivo biodistribution and highly efficient tumour targeting of carbon nanotubes in mice. *Nat.*
224 *Nanotechnol.* **2**, 47-52 (2007).

225 22 Gao, Z., Varela, J. A., Groc, L., Lounis, B. & Cognet, L. Toward the suppression of cellular toxicity from
226 single-walled carbon nanotubes. *Biomater. Sci.* **4**, 230-244 (2016).

227 23 Santos, S. M. *et al.* All-optical trion generation in single-walled carbon nanotubes. *Phys. Rev. Lett.* **107**,
228 187401 (2011).

229 24 Thorne, R. G. & Nicholson, C. In vivo diffusion analysis with quantum dots and dextrans predicts the
230 width of brain extracellular space. *Proc. Natl. Acad. Sci. U.S.A.* **103**, 5567-5572 (2006).

231 25 Han, Y. *et al.* Brownian motion of an ellipsoid. *Science* **314**, 626-630 (2006).

232 26 Schutz, G. J., Schindler, H. & Schmidt, T. Single-molecule microscopy on model membranes reveals
233 anomalous diffusion. *Biophys. J.* **73**, 1073-1080 (1997).

234 27 Tardin, C., Cognet, L., Bats, C., Lounis, B. & Choquet, D. Direct imaging of lateral movements of AMPA
235 receptors inside synapses. *EMBO J.* **22**, 4656-4665 (2003).

236 28 Kusumi, A., Sako, Y. & Yamamoto, M. Confined lateral diffusion of membrane receptors as studied by
237 single particle tracking (nanovid microscopy). Effects of calcium-induced differentiation in cultured
238 epithelial cells. *Biophys. J.* **65**, 2021-2040 (1993).

239 29 Godin, A. G., Lounis, B. & Cognet, L. Super-resolution microscopy approaches for live cell imaging.
240 *Biophys. J.* **107**, 1777-1784 (2014).

241 30 Kochlamazashvili, G. *et al.* The extracellular matrix molecule hyaluronic acid regulates hippocampal
242 synaptic plasticity by modulating postsynaptic L-type Ca(2+) channels. *Neuron* **67**, 116-128 (2010).

243

244 **Acknowledgements.** We warmly thank E. Bézard, M. Blanchard-Desce, B. Bontempi and P. Bon
245 for helpful discussions. We thank J.P. Salvétat for experimental help for AFM imaging, and
246 J. Ferreira for support with histological experiments. This work was supported by CNRS,
247 Agence Nationale de la Recherche (ANR-14-OHRI-0001-01), IdEx Bordeaux (ANR-10-IDEX-
248 03-02), Labex Brain (ANR-10-LABX-43), Conseil Régional d'Aquitaine (2011-1603009) and
249 the France-BioImaging national infrastructure (ANR-10-INBS-04-01). A.G.G. acknowledges
250 financial support from the Fondation pour la Recherche Médicale and the Fonds Recherche du
251 Québec – Nature et Technologies. J.A.V. acknowledges Marie Curie Individual Fellowship
252 326442 funding.

253 **Author contributions statement.** A.G.G., J.A.V., Z.G. and J.P.D. performed the experiments.
254 A.G.G., N.D., B.L. and L.C. performed the analysis. B.L., L.G. and L.C. co-supervised the study.
255 L.G. and L.C. designed the study. All authors discussed the results and co-wrote the manuscript.

256 **Competing financial interest statement.** We declare no competing financial interests.

257 **Additional information.** Supplementary information is available in the online version of the
258 paper. Reprints and permission information is available online at www.nature.com/reprints.
259 Correspondence and requests for materials should be addressed to L.C. ([laurent.cognet@u-](mailto:laurent.cognet@u-bordeaux.fr)
260 [bordeaux.fr](mailto:laurent.cognet@u-bordeaux.fr)) & L.G. (laurent.groc@u-bordeaux.fr). Analysis codes used in this study are
261 available upon request to L.C. or L.G.

262

263 **Figure caption**

264 **Figure 1. Single molecule tracking of luminescent SWCNTs in live ECS brain tissue.**

265 (a) SWCNTs are injected in lateral ventricles of living rats and diffuse into the neocortex.
266 (b) Luminescent SWCNTs are imaged in brain slices. (c) Absorbance spectrum of 1 mm thick
267 brain slice (black) and photoluminescence spectrum of a single (6,5) SWCNT in the ECS (red)
268 upon 845 nm laser excitation (purple). (c, inset) Photoluminescence image of a (6,5) SWCNT
269 recorded in the ECS with its orientation θ . (d) Color-coded trajectory of a single SWCNT
270 diffusing in live ECS (20,000 data points). Scale bars = 1 μm .

271 **Figure 2. SWCNT diffusion properties in the ECS. (a) $\text{MSD}_{x,y}(\tau)$ in the laboratory frame**

272 (black squares) and $\text{MSD}_{\parallel,\perp}(\tau)$ calculated along (blue circles) and perpendicular (red diamonds)
273 to the SWCNT axis for a 2D trajectory recorded in the ECS. Purple crosses correspond to
274 $\text{MSD}_{\parallel} + \text{MSD}_{\perp}$. (b) Evolution of the mean MSDs for the slow diffusion states
275 $\langle \mathbf{r}_{\parallel,\perp}^2 \rangle_1(\tau)$ retrieved from the analysis of the DSDs. The plateau of $\langle \mathbf{r}_{\perp}^2 \rangle_1(\tau)$ gives an average
276 ECS domain size $\langle \xi \rangle$ of 160 nm. (c) Histograms of $\langle \xi \rangle$ values measured from all single SWCNT
277 trajectories as in (b). (d) Schematic representation of a SWCNT diffusing in the ECS.

278 **Figure 3. Super-resolution imaging of ECS morphology and ECS local viscosity maps.**

279 (a) Super-resolved image of live brain ECS morphology obtained from 20,000 localizations of a
280 diffusing SWCNT. Scale bar = 500 nm. (b) Histogram of ECS domain dimensions ξ (N = 419)
281 from 14 ECS super-resolved images as in (a). (c) Spatial map of SWCNT instantaneous diffusion
282 coefficients calculated along the same trajectory using a sliding window of 300 ms. This
283 representation also constitutes a high-resolution spatial map of ECS viscosities (see scale bar).

284 **Figure 4. ECS local modifications in chemically altered brains.** Representative images of

285 HAPB immunostaining in brain slices from naïve (a) and hyaluronidase-injected rats (altered, b).
286 Neuronal nuclei are labelled with DAPI (blue). Scale bar: 250 μm . High magnification spinning
287 disk microscope images of HAPB staining in both conditions are also presented (c, d). Scale bar:
288 20 μm . (e) Examples of super-resolved ECS images of naïve vs. altered live brain tissues. Scale
289 bars: 2 μm . (f) Areas explored normalized by SWCNT trajectory lengths. (g) Corresponding
290 spatial viscosity maps. (h) Histograms of all instantaneous diffusion coefficients. In naïve brains,
291 the distribution is fitted with a single log-normal distribution ($0.08 \pm 0.08 \mu\text{m}^2/\text{s}$, median \pm s.d.)

292 while in altered brains, two independent log-normal distributions are needed ($0.09 \pm 0.11 \mu\text{m}^2/\text{s}$ &
293 $0.28 \pm 0.26 \mu\text{m}^2/\text{s}$). (i) Average ECS domain dimensions $\langle \xi \rangle$ as in Figure 2e for the two
294 conditions. Statistical tests are two-tailed unpaired Mann-Whitney t-test ** $p < 0.01$.

295

296 **Methods**

297 **SWCNT preparation.** PL-PEG preparation. HiPco synthesized nanotubes (batch no. 195.7
298 bought from Rice University) were suspended by biocompatible phospholipid-polyethylene
299 glycol (PL-PEG) molecules (#MPEG-DSPE-5000, [Laysan Bio, Inc.](#)) which prevent nonspecific
300 biomolecules absorption, minimize nanotubes sticking, and allow nanotubes diffusion in live
301 tissue¹⁻²: 2 mg of raw SWCNTs and 100 mg PL-PEG were added in 2 ml Milli-Q water and
302 dispersed by tip sonication (6W output for 3 minutes). Nanotubes bundles and impurities were
303 precipitated by centrifuging the dispersion at 10,000 rpm for 60 min at 4°C. The supernatant was
304 collected and stored at 4°C for brain injection within 48 hours. The concentration of PL-PEG
305 SWCNT solution was estimated to 3 $\mu\text{g}/\text{ml}$. From the two-dimensional photoluminescence
306 excitation/emission map of the injected SWCNT solution ([Figure S15](#)), the subpopulation of
307 (6,5) SWCNTs is estimated to represent 3-5% of the total population, such that SWCNTs
308 detected in the brain slices at low density, are not affected by other chiralities. PL-PEG-NH₂
309 preparation: SWCNT were also suspended by biocompatible phospholipid-polyethylene glycol-
310 amine (PL-PEG-NH₂) molecules (#MPEG-DSPE-NH₂-5000, Laysan Bio, Inc.): 1 mg of raw
311 SWCNTs and 15 mg PL-PEG-NH₂ were added in 1 mL Milli-Q water and 0.5 ml Deuterium
312 Oxide and dispersed by tip sonication (8 W output for 30 seconds). Nanotubes bundles and
313 impurities were precipitated by centrifuging the dispersion at 10,000 rpm for 45 min at 4 °C. The
314 supernatant was collected and stored at 4 °C for experiments (0.4 $\mu\text{g}/\text{mL}$).

315

316 **Intraventricular injections.** Sprague-Dawley rats (Janvier, France) were used for this work,
317 both male and female, treated according to the guidelines of the University of Bordeaux/CNRS
318 Animal Care and Use Committee. Injections of SWCNTs were performed in living Sprague-
319 Dawley rat pups (1-4 days old) anesthetized by hypothermia. Approximately 5 μl of SWCNTs
320 dispersion were injected in each lateral ventricle (12 rats). Under cold light illumination, the
321 injection place was found by firstly drawing a virtual line between the eye and lambda (easily
322 seen through the skin), secondly finding the midpoint of that line, and thirdly moving 2 mm

323 caudal from that mid-point along the virtual line. The injection was performed in that point, at a
324 depth of 2.6 mm for P1 pups, 2.9 mm for P2 pups, 3.1 mm for P3 pups and 3.5 mm for P4 pups.
325 For hyaluronidase studies the intraventricular injection was performed in the same way (3 rats),
326 injecting hyaluronidase from bovine testes 20 mg/mL in PBS (Sigma Aldrich #H3506) the night
327 before injecting SWCNT.

328

329 **Acute brain slices preparation.** Between 10 min and up to 3 h after SWCNT injection, pups
330 were decapitated and parasagittal brain slices (0.5 mm thick) were prepared in an ice-cold
331 artificial cerebrospinal fluid (ACSF) solution containing (in mM): 126 NaCl, 3.5 KCl, 2 CaCl₂,
332 1.3 MgCl₂, 1.2 NaH₂PO₄, 25 NaHCO₃, and 12.1 glucose (gassed with 95% O₂ / 5% CO₂; pH
333 7.35). Slices were then imaged in oxygenated ACSF at 33°C perfused in the imaging chamber
334 with a peristaltic pump.

335

336 **Immunostainings.** Staining of Iba1, Aggrecan and HABP were performed in coronal brain
337 slices of 80 µm thickness. Before antibody incubation, slices were incubated with PBS-Triton-
338 X100 1% and 4% BSA for 2h under agitation at room temperature. Slices were subsequently
339 washed three times with PBS for 5 min each time. Slices were incubated overnight at 4 °C with
340 primary antibodies in PBS-Triton-X100 0.2% and 2% BSA solution. Anti-Iba1 rabbit antibody
341 (Wako Pure Chemical Industries #019-19741) was used at a 1:200 dilution. Anti-Aggrecan
342 rabbit antibody (Millipore #AB1031) was used at a 1:200 dilution. Biotinilated HABP (Amsbio
343 #AMS.HKD-BC41) was also used at a 1:200 dilution. Slices were subsequently washed three
344 times with PBS for 5 min each time, and incubated with secondary reagents. Anti-Iba1 and anti-
345 Aggrecan antibodies were labelled with goat anti-rabbit Alexa568 (ThermoFisher Scientific #A-
346 11011) in PBS-Triton-X100 0.2% and 2% BSA solution for 2h at room temperature under
347 agitation, at a 1:1000 dilution. Biotinilated HABP was labelled with Alexa568 streptavidin
348 (ThermoFisher Scientific #S11226) in PBS-Triton-X100 0.2% and 2% BSA solution for 2h at
349 room temperature under agitation, at a 1:1000 dilution. Slices were finally washed three times
350 with PBS and mounted in glass slides with Vectashield+DAPI (Vector Labs).

351

352 **Organotypic slice preparation.** Organotypic slice cultures were prepared as previously
353 described³. Briefly, 350 µm thick hippocampal slices were obtained from postnatal day 5 to

354 postnatal day 7 Sprague-Dawley rats using a McIlwain tissue chopper, and were placed in a pre-
355 heated (37°C) dissection medium containing (in mM): 175 sucrose, 25 D-glucose, 50 NaCl, 0.5
356 CaCl₂, 2.5 KCl, 0.66 KH₂PO₄, 2 MgCl₂, 0.28 MgSO₄·7H₂O, 0.85 Na₂HPO₄·12H₂O, 2.7
357 NaHCO₃, 0.4 HEPES, 2 x 10⁻⁵ % phenol red, pH 7.3 (all products from Sigma unless specified).
358 After 25 min of incubation, slices were transferred on white FHLC membranes (0.45 μm) set on
359 Millicell Cell Culture Inserts (Millipore, 0.4 mm; Ø 30 mm), and cultured for up to 14 days on
360 multiwell-plates at 35°C / 5% CO₂ in a culture medium composed of 50 % Basal Medium Eagle,
361 25 % Hank's balanced salt solution 1X (with MgCl₂ / with CaCl₂), 25 % heat-inactivated horse
362 serum, 0.45 % D-glucose, 1 mM L-glutamine (all products from Gibco unless specified). The
363 medium was changed every 2-3 days.

364
365 **Single cell electroporation.** Electroporation of single pyramidal neurons was performed as
366 previously described⁴. Briefly, individual CA1 pyramidal neurons from 4-6 days in vitro
367 hippocampal slices were electroporated to transfect cDNA encoding EGFP. Plasmids (5 μl at
368 1 μg/μl) were dissolved in a filtered cesium-based solution containing (in mM): 135 cesium-
369 methanesulfonate, 8 NaCl, 10 HEPES, 0.2 EGTA, 4 Na₂ATP, 0.33 Na₃GTP,
370 5 tetraethylammonium chloride, pH 7.3 (all products from Sigma unless specified). This solution
371 was supplemented with 10 μL of filtered endotoxin-free buffer TE (Qiagen), then centrifuged
372 twice to pull down potential debris (10000 rpm, 15 min, 4°C) and used to fill 5-6 MΩ
373 borosilicate patch pipettes. Electroporation was performed in 2 mL of pre-warmed (37°C / 5%
374 CO₂) HEPES-based artificial cerebrospinal fluid (ACSF) containing (in mM): 130 NaCl, 2.5
375 KCl, 2.2 CaCl₂, 1.5 MgCl₂, 10 HEPES, 10 D-glucose. Plasmid transfer was allowed by the
376 delivery of 50 μs-width square-pulses at 100 Hz (1 s duration; -14 V current amplitude).

377
378 **COS-7 cell culture.** COS-7 cells were grown in Dulbecco's Modified Eagle Medium (DMEM)
379 without phenol-red (PAN Biotech, P04-01515) supplemented with 10% v/v foetal calf serum
380 (FCS-Dominique Dutscher, 500105), 1% v/v penicillin/streptomycin (Dominique Dutscher, P06-
381 07100) in 25 mL flasks (Falcon, 353082) at 37 °C, 5% CO₂. They were kept below 90%
382 confluence, at which cells were washed in sterile filtered PBS (PAN Biotech, P04-36500),
383 detached in a small volume of trypsin (PAN Biotech, P10-021100), washed in full warm medium
384 and split 1/10 in a new flask. For imaging, 90% confluent cells were similarly detached with

385 trypsin and diluted 1/10 in full warm medium. COS7 cells were plated in uncoated petri dish. 24
386 hours after the plating, nanotubes were added (10 μ l of the 3 mg/L PL-PEG nanotube solution
387 and 60 μ l of the 0.4 mg/L PL-PEG-NH₂ nanotube solution) to 1 mL of medium for 1h. The
388 samples were rinsed 3 times for 5 minutes with medium and imaged under the fluorescent
389 microscope.

390
391 **Wide-field Fluorescence Microscopy Setup.** Single SWCNT photoluminescence imaging was
392 performed with an inverted microscope equipped with an electron-multiplying CCD camera
393 (Princeton Instruments ProEm) and a 1.45 NA 60x objective in a wide-field geometry. The
394 excitation source consisted of a tunable Ti:Sa laser emitting at a wavelength of 845 nm to
395 preferentially excite (6,5) SWCNTs at the resonance of the dark K-momentum exciton⁵. The
396 excitation intensity was kept at 10 kW/cm² with circularly polarized light. A dichroic mirror
397 (FF875-Di01, Semrock) and a long-pass emission filter (ET900LP, Chroma) were used in order
398 to illuminate and detect the SWCNT emitted fluorescence. Images of SWCNTs were recorded at
399 40 or 50 frames per second (typically 20,000 frames). GFP/Alexa488 (Excitation : FF02-
400 472/30, Dichroic : FF495-Di03 and emission : FF01-520/35) and DAPI (Excitation : FF01-
401 387/11, Dichroic : FF409-Di03 and emission : FF02-447/60) were imaged using epifluorescence
402 white light excitation with appropriate filter sets.

403
404 **Spinning disk microscope.** Alexa568 imaging in acute slices was performed in a Leica
405 DMI6000 inverted microscope (Leica Microsystems) with a Yokogawa spinning disk unit CSU-
406 X1. The setup was equipped with live cell chamber and temperature was constantly kept at 37
407 °C. Tissue scans were obtained with either 10x air, 63x oil and 100x oil objectives, with
408 exposure times of 50-100ms per frame. DAPI staining in fixed tissue was excited with a 405nm
409 laser line, and detected through a standard DAPI emission filter. Images were acquired using an
410 Evolve EM-CCD camera (Photometrics), setting the EM gain at 600.

411
412 **NIR Spectrometer Setup.** Emission spectra of single SWCNTs were collected using a
413 cryogenically cooled 1D InGaAs detector (OMA V, Roper Scientific) placed at the output of a
414 150 mm spectrometer. A Chameleon (Coherent) pumped with a Ti:Sapphire laser (spectral range
415 of 530-700 nm) and a Ti:Sa laser (spectral range of 700 to 850 nm) were used to generate a two-

416 dimensional photoluminescence excitation/emission map of the PL-PEG SWCNT solution.
417 Individual spectra of the nanotube solution, in a 1 cm long quartz cuvette, were normalized by
418 the incident power. The spectrum of a solution containing only surfactant, acquired under the
419 same experimental condition, was subtracted for each laser wavelength. The proportion of
420 nanotubes (6,5) in the solution was estimated by comparing the peak value for detected semi-
421 conducting chiralities and assuming ~30% of metallic chiralities in HiPco samples.

422
423 **Single cell loading.** Single CA1 pyramidal neurons from 4-8 days in vitro (div) hippocampal
424 organotypic slices were loaded with dilutions of carbon nanotubes to allow monitoring of their
425 intracellular motion patterns. Briefly, nanotubes were dissolved (1/100 dilution) in a filtered
426 cesium-based solution containing (in mM): 135 cesium-methanesulfonate, 8 NaCl, 10 HEPES,
427 0.2 EGTA, 4 Na₂ATP, 0.33 Na₃GTP, 5 tetraethylammonium chloride, pH 7.3 (all products from
428 Sigma unless specified). This solution was supplemented with Alexa-488 (20 µg/mL) to allow
429 further visual detection of the neurons of interest and used to fill 5-6 MΩ borosilicate patch
430 pipettes. Single-cell loading was performed in 2 mL of pre-warmed (37°C / 5% CO₂) HEPES-
431 based artificial cerebrospinal fluid (ACSF) containing (in mM): 130 NaCl, 2.5 KCl, 2.2 CaCl₂,
432 1.5 MgCl₂, 10 HEPES, 10 D-glucose. Nanotube transfer from the cesium-based solution to the
433 cytoplasm was allowed by patching pyramidal neurons in whole-cell configuration.

434
435 **Determination of SWCNT localization and orientation.** Two-dimensional Gaussian functions
436 with an arbitrary orientation were used to fit SWCNT images using homemade MatLab routines
437 and determine SWCNT localizations (x_i, y_i), orientation θ_i , as well as large and small radii of
438 the SWCNT image. Four consecutive images were averaged for each fit to improve localization
439 precision (40 nm). SWCNT coordinates are then interconnected to reconstruct nanotube
440 trajectories. When available, the positions of an immobile SWCNT was used to correct eventual
441 small stage drifts over the 10 min recordings. Orientations ($\theta \in [0, \pi]$) obtained from the
442 Gaussian fits are by construction doubly degenerate. The SWCNT orientation on the first image
443 of the movie is assumed to be between $[0, \pi]$. This choice sets which end of the SWCNT is
444 considered as the front of the tube. For all other orientations, continuity arguments are used to
445 remove this degeneracy and to allow the orientation to be a real unbounded physical quantity
446 ($\theta \in [-\infty, \infty]$).

447

448 **Super-resolved images of the ECS from SWCNT localizations.** For each trajectory, a super-
449 resolved image of the ECS was computed by cumulating all SWCNT localizations (typically
450 20,000 points). In super-resolved images, each localization is displayed a two-dimensional
451 Gaussian of 50 nm width and unit amplitude as commonly used in localization microscopy⁶.

452

453 **Estimation of SWCNT lengths.** For each SWCNT trajectory imaged in live brain ECS, the
454 distribution of eccentricity, obtained from the 2D asymmetric Gaussian fits of the nanotube
455 images, was calculated when nanotube movements were undetectable (displacements between
456 images < 40 nm). For each trajectory, the mean of the distribution was then used to determine the
457 nanotube length (Figure S10) by comparison to the following model: the photoluminescence
458 profile of a rigid nanotube of varying length L emitting at 986 nm was modelled as previously⁷
459 using exciton diffusion length of ≈ 100 nm to provide a look-up table.

460 **Atomic force microscopy** (Figure S10b&c). PL-PEG SWCNTs were spin-coated on plasma-
461 cleaned glass coverslips using a G3P-8 Spin coater (Specialty Coating Systems) at 930 rpm for 3
462 min. To remove excess PL-PEG, samples were rinsed using Milli-Q water. Atomic force
463 microscopy (AFM) images were recorded using an 8 nm diameter Si₃N₄ tip. For each well
464 isolated SWCNT, the length was quantified using the NeuronJ plugin in ImageJ⁸.

465

466 **Mean squared displacements (MSD) analysis (Figure 2a).** For each trajectory, three Mean
467 Squared Displacement (MSD) curves were calculated as exemplified in Figure 2a: (i) MSD_{xy} in
468 the laboratory frame corresponding to 2D movements in the imaging plane, and (ii) MSD_{\parallel} and
469 MSD_{\perp} by decoupling 1D movements along (\parallel) and perpendicular (\perp) to the nanotube axis.

470 In order to decouple the diffusion of SWCNTs along and perpendicular to their principal
471 axis, the displacement vector $(x_{i+1} - x_i, y_{i+1} - y_i)$ was determined at time t_{i+1} from the
472 projection on the nanotube orientation vector obtained at time t_i (see inset of Figure 2a). This
473 procedure to decouple the movements along and perpendicular to anisotropic object axis was
474 presented previously⁹⁻¹⁰. One dimensional MSD_{\parallel} and MSD_{\perp} could then be calculated from
475 decoupled displacements (Figure 2a).

476 For one dimensional free diffusion, MSD curves are linear with time, with a slope equal to
 477 2D. More precisely, $MSD(\tau) = \langle r^2 \rangle(\tau) = \int_{-\infty}^{+\infty} x^2 c(x, \tau) dx = 2D\tau$, where D is the diffusion
 478 coefficient and $c(x, t)$ represents the probability of finding nanotubes at position x at time t if all
 479 nanotubes would be initially placed at $x=0$. $c(x, t)$ is the solution to the one dimensional
 480 diffusion equation $\frac{\partial c(x,t)}{\partial t} = D \frac{\partial^2 c(x,t)}{\partial x^2}$ and equals $c(x, t) = \frac{N}{\sqrt{4\pi Dt}} e^{-x^2/4Dt}$, where N is the
 481 number of particles in the system.

482 Similarly, for two dimensional free diffusion, the MSD slope is equal to 4D since the MSD
 483 equals $MSD(\tau) = \langle r^2 \rangle(\tau) = \int_0^{+\infty} \rho^2 c(\rho, \tau) d\rho = 4D\tau$ where $c(\rho, t)$ is the solution of the two
 484 dimensional diffusion equation.

485 When the MSDs are not linear with time, a diffusion coefficient can be defined from the
 486 initial slopes of $\langle r^2 \rangle(\tau)$ determined on short times.

487
 488 **Distribution of squared displacements (DSD) and calculation of $\langle \xi \rangle$ (Figures 2b-c, 4i**
 489 **and S11).** Considering a diffusing particle, the cumulative distribution of squared displacements
 490 ($DSD^\tau(r^2)$) represents the probability of finding the particle at a distance less than r from its
 491 initial position after a time lag τ .

492 In the case of a freely diffusing particle along one coordinate, it is given by:

$$493 \quad DSD^\tau(r^2) = \frac{\int_{-r}^{+r} c(x, \tau) dx}{\int_{-\infty}^{+\infty} c(x, \tau) dx} = \text{erf}\left(\sqrt{r^2/4D\tau}\right) = \text{erf}\left(\sqrt{r^2/2\langle r^2 \rangle(\tau)}\right).$$

494 In the case of a mixture of particles following two distinct 1D diffusion behaviours (*e.g.*
 495 free diffusion with D_1 and D_2), the DSD is characterized summing two independent diffusive
 496 processes:

$$497 \quad DSD^\tau(r^2) = \sum_{i=1}^2 \alpha_i \cdot \text{erf}\left(\sqrt{r^2/2\langle r^2 \rangle_i(\tau)}\right), \quad (\text{EQ1})$$

498 where α_i are the fraction of particles in the different diffusive states (in the case of free
 499 diffusion : $\langle r^2 \rangle_i(\tau) = 2D_i\tau$).

500 A similar analysis was previously used to retrieve different molecular populations bearing
 501 distinct 2D diffusion behaviours from the observation of many short trajectories¹¹⁻¹².

502 Here a single and long trajectory of diffusing SWCNT displaying different temporal
 503 diffusive behaviours along its course is analysed. In order to retrieve the different diffusive

504 behaviours, the DSD analysis was performed on the displacements along and perpendicular to
505 SWCNT axes.

506 From single trajectories, the cumulative distribution of squared displacement along each
507 direction (parallel and perpendicular to the nanotube axis) was computed for every time lag (see
508 examples in Figure S11 for the trajectory analysed in Figures 2 and 3). Each line corresponds to
509 the experimental DSDs at a given time lag τ . Values of α_j and $\langle r^2 \rangle_j$ were estimated by fitting
510 Equation EQ1 in each line. Two different diffusing processes were systematically retrieved from
511 the global fitting procedure along each direction ($\langle r_{\perp,\parallel}^2 \rangle_{1,2}$). The evolutions $\langle r_{\perp,\parallel}^2 \rangle_{1,2}$ are
512 presented in Figure S11C&D as a function of the time lag τ .

513 The evolution of $\langle r_{\perp}^2 \rangle_{\perp}$ is the slowest and displays a saturation revealing a confinement of
514 the transverse movements of SWCNTs in the ECS. The typical ECS dimension responsible for
515 this confinement can be estimated from the saturation value of $\langle r_{\perp}^2 \rangle_{\perp} : \langle \xi \rangle = \sqrt{6 \langle r_{\perp}^2 \rangle_{\perp}^{sat}}^{13}$.

516
517 **Two-dimensional spatial maps of instantaneous diffusion coefficients and ECS local**
518 **viscosity (Figures 3c, 4g&h and Extended Data movies 1 and 2).** In order to create diffusion
519 coefficient spatial maps, MSDs were calculated in the laboratory frame using a sliding window
520 of 300 ms along each trajectory instead of the full trajectory as above. Linear fits of the initial
521 slopes of the sliding MSDs were performed on the first 100 ms to obtain the instantaneous
522 diffusion coefficients D_{xy} as a function of time. Values of instantaneous diffusion coefficients
523 were obtained for each subset of detections ($t_0 - 150 \text{ ms} \leq t \leq t_0 + 150 \text{ ms}$) and associated to
524 the centroid position (Figure 3c, 4e,g&h). Maps were created using pixels of 25 nm.
525 Instantaneous diffusion coefficients falling within the same pixel were averaged. For
526 visualization purposes, convolution with a two dimensional Gaussian of 50 nm FWHM was
527 applied to smooth the data.

528 In order to link instantaneous diffusion coefficient values of the SWCNTs to local
529 viscosities of the ECS, we used the relationship between the diffusion coefficient of highly
530 anisotropic rods diffusing in a 2D plane and the viscosity¹⁴ : $\eta = 3k_B T \ln(\phi) / (8\pi D_{xy} L)$. The
531 nanotube length was estimated for each trajectory using the eccentricity of the imaged nanotube
532 (see above).

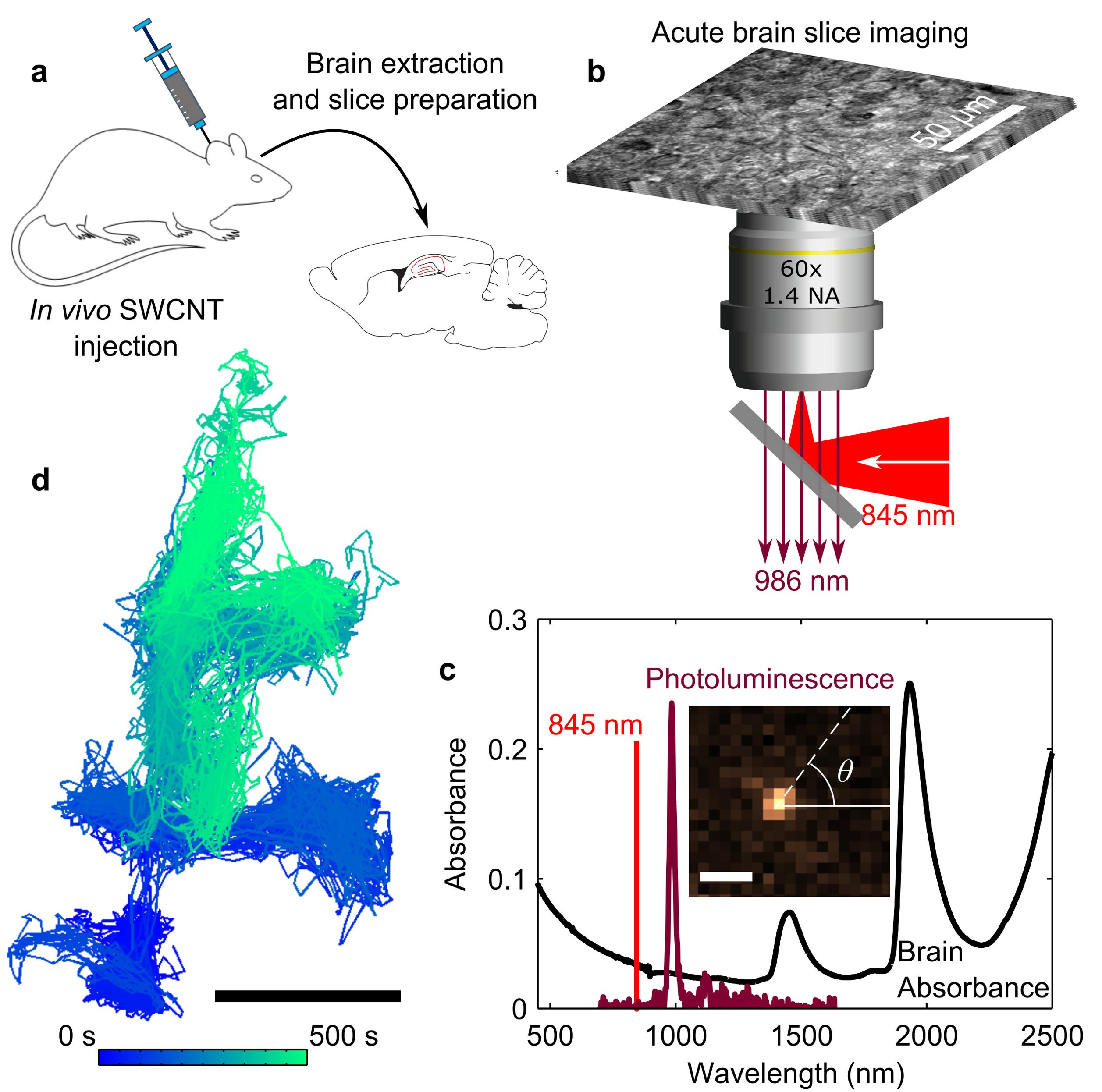
533

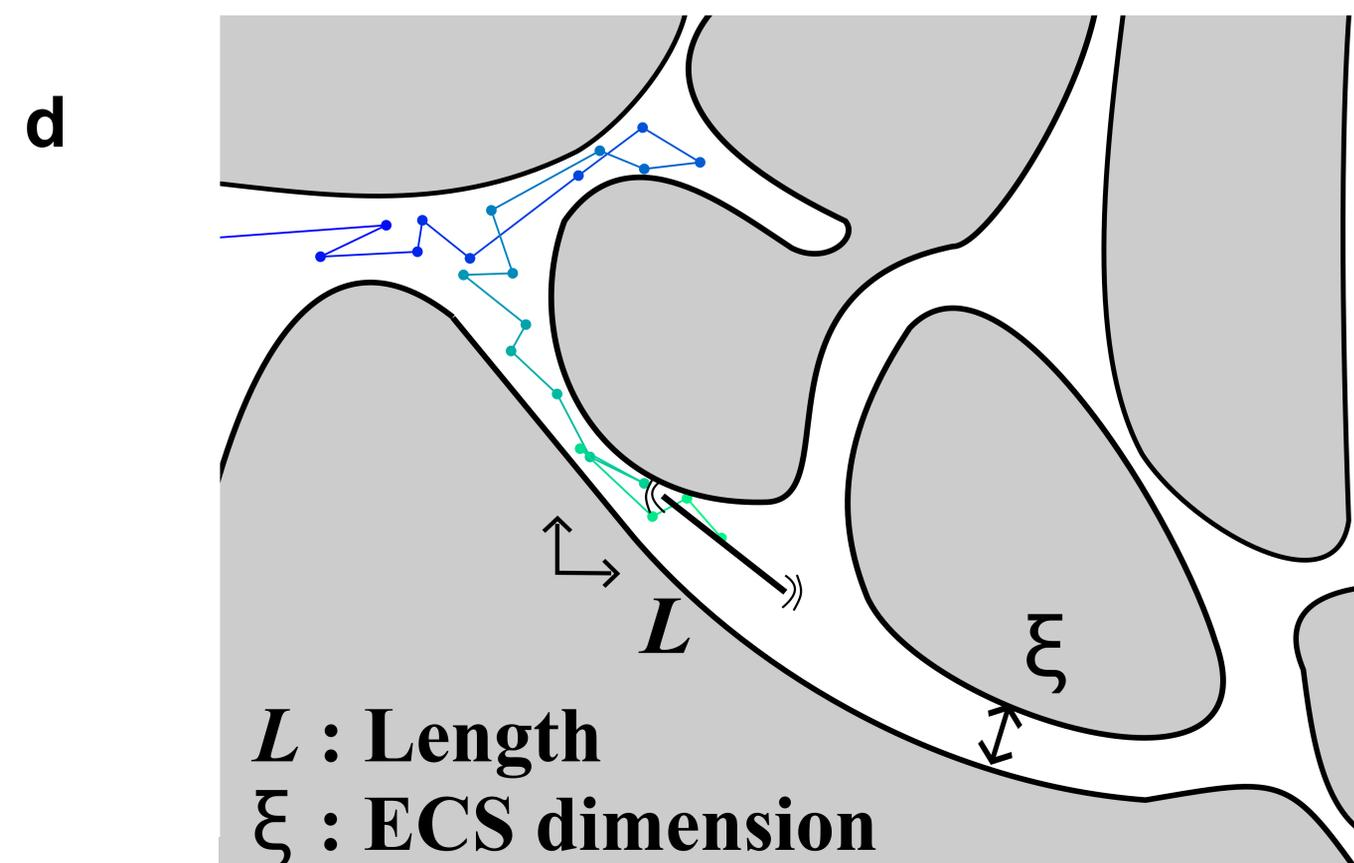
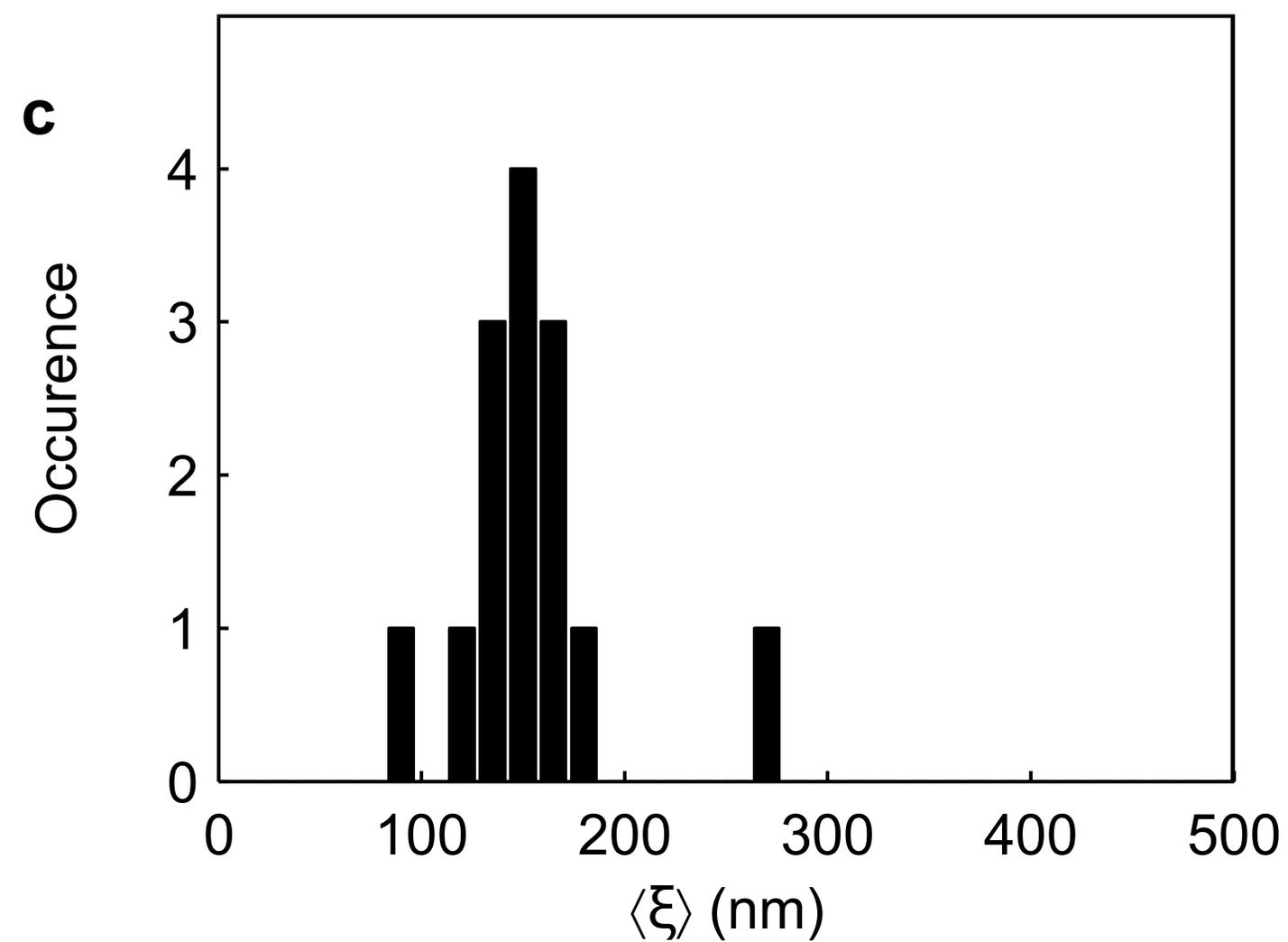
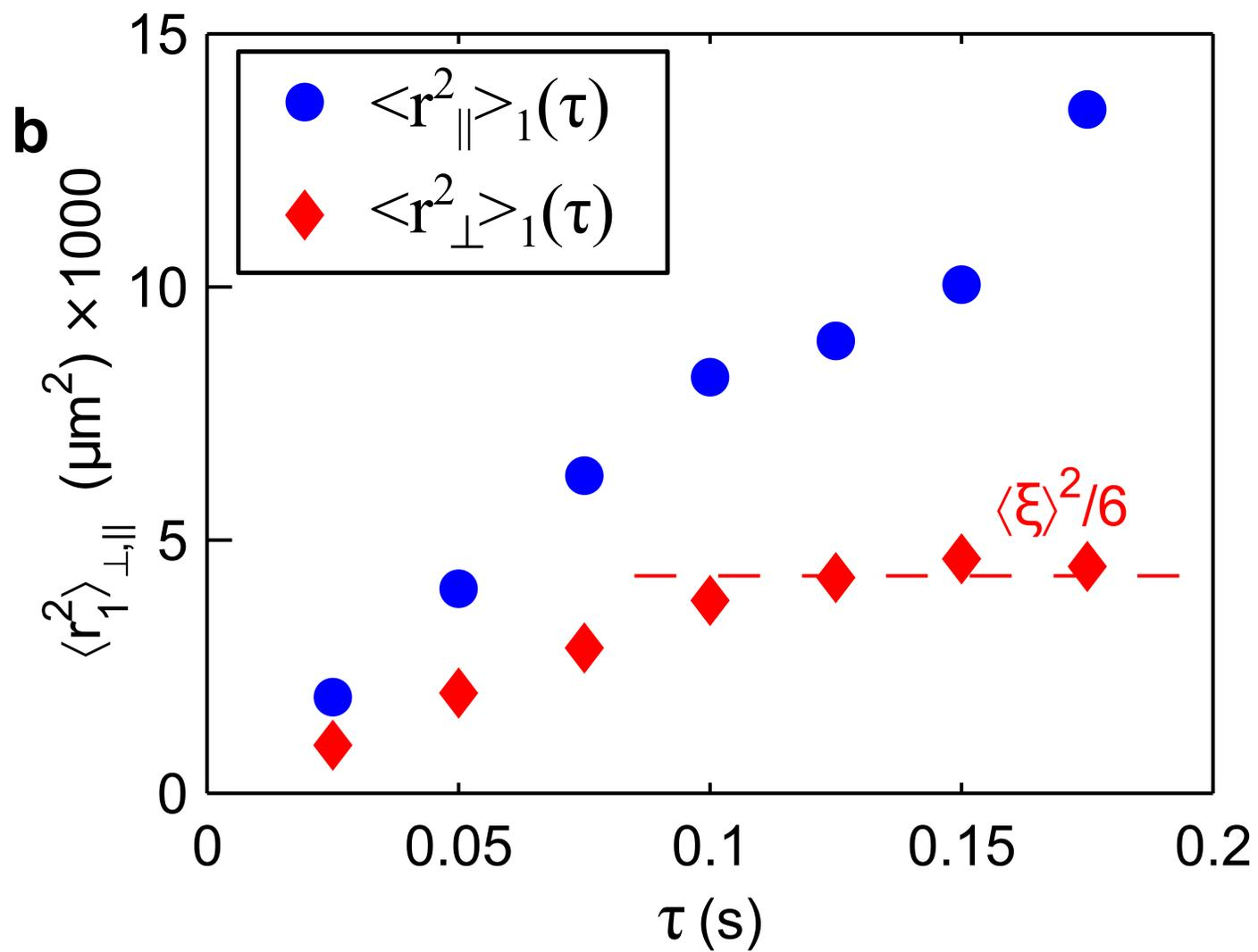
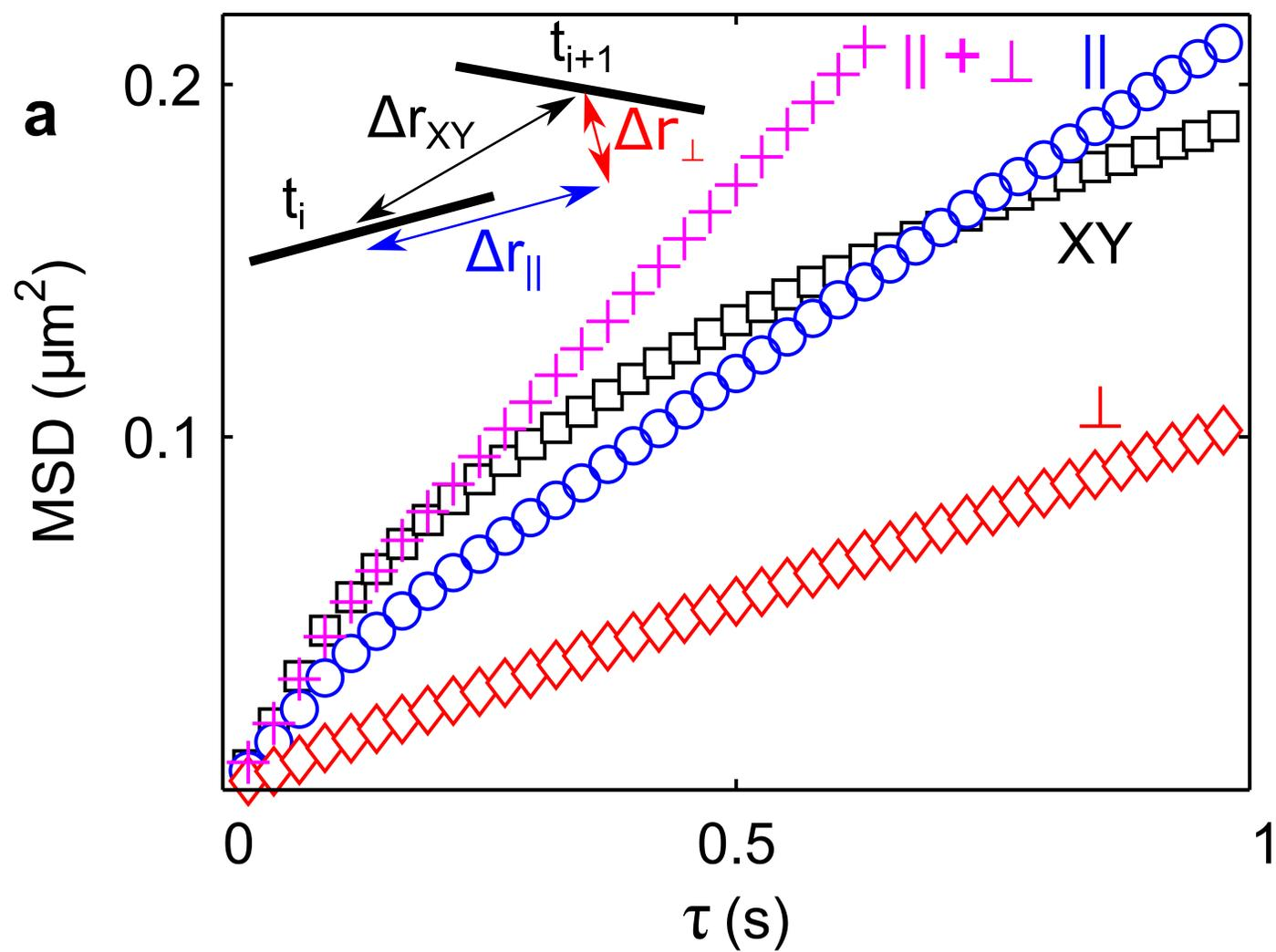
534 **Estimation of the ECS dimensions from the analysis of super-resolved images (Figure 3b**
535 **and Figure S12).** Super-resolved images revealed the diversity and complexity of the ECS
536 morphology. In order to measure the typical dimensions of the ECS, we applied a global analysis
537 by using a set of 2D Gaussian functions to directly fit the SWCNT localizations used to create
538 the super-resolved images (Figure S12b). Initial guesses for applying Gaussian fitting was based
539 on local density maxima of nanotube localizations (Figure S12a, inset & c). Two maxima that
540 were closer than 75 nm could not induce two different Gaussian functions. The transverse
541 dimensions of the set of 2D Gaussian functions used to fit the nanotube localizations provides
542 the dimensions ξ of the ECS displayed in Figures 3b and S12a.

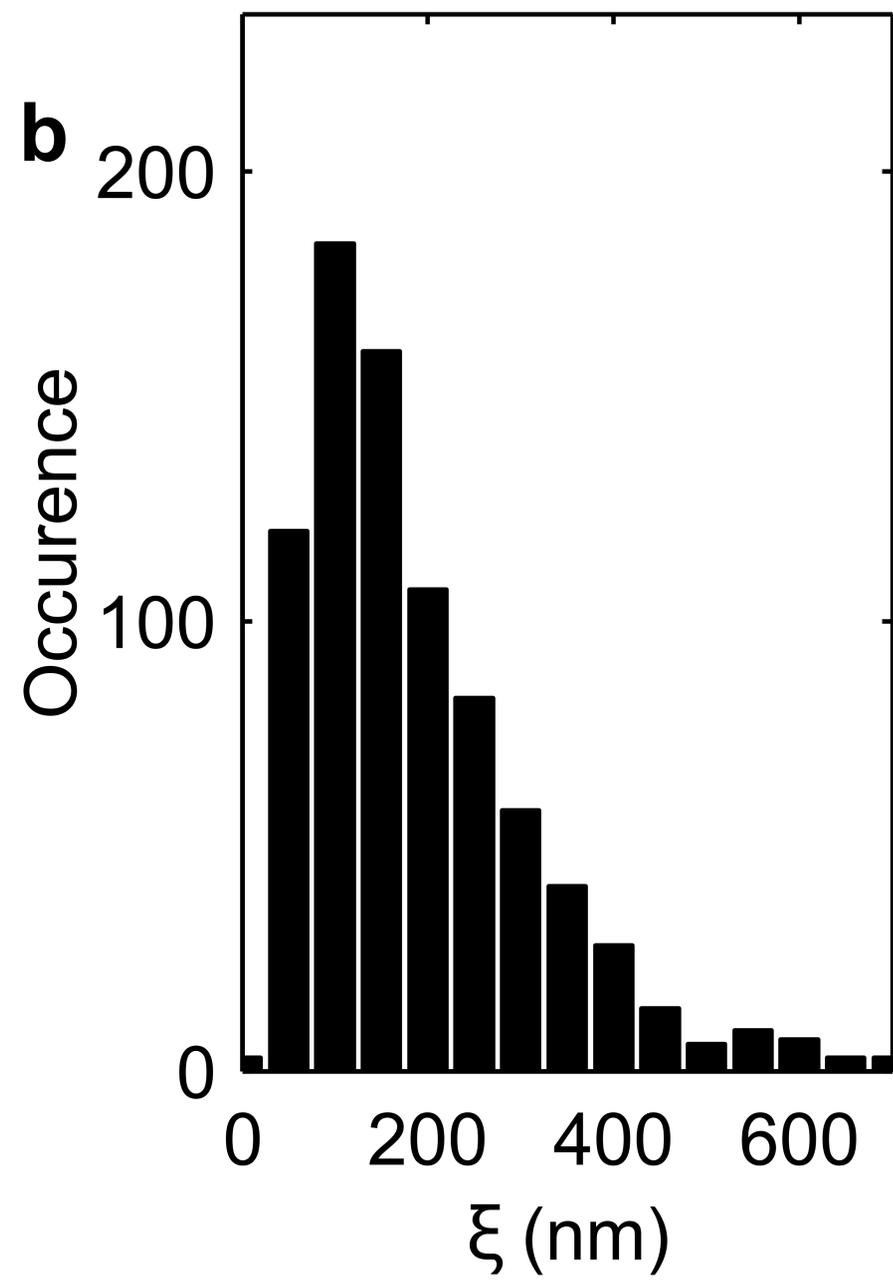
543 **References for the Methods section:**

- 544 1 Liu, Z. et al. In vivo biodistribution and highly efficient tumour targeting of carbon
545 nanotubes in mice. *Nat. Nanotechnol.* 2, 47-52 (2007).
- 546 2 Gao, Z., Varela, J. A., Groc, L., Lounis, B. & Cognet, L. Toward the suppression of
547 cellular toxicity from single-walled carbon nanotubes. *Biomater. Sci.* 4, 230-244 (2016).
- 548 3 Stoppini, L., Buchs, P. A. & Muller, D. A simple method for organotypic cultures of
549 nervous tissue. *J Neurosci Methods* 37, 173-182 (1991).
- 550 4 Haas, K., Sin, W. C., Javaherian, A., Li, Z. & Cline, H. T. Single-cell electroporation for
551 gene transfer in vivo. *Neuron* 29, 583-591 (2001).
- 552 5 Santos, S. M. et al. All-optical trion generation in single-walled carbon nanotubes. *Phys.*
553 *Rev. Lett.* 107, 187401 (2011).
- 554 6 Godin, A. G., Lounis, B. & Cognet, L. Super-resolution microscopy approaches for live
555 cell imaging. *Biophys. J.* 107, 1777-1784 (2014).
- 556 7 Oudjedi, L., Parra-Vasquez, A. N., Godin, A. G., Cognet, L. & Lounis, B. Metrological
557 Investigation of the (6,5) Carbon Nanotube Absorption Cross Section. *J. Phys. Chem.*
558 *Lett.* 4, 1460-1464 (2013).
- 559 8 Meijering, E. et al. Design and validation of a tool for neurite tracing and analysis in
560 fluorescence microscopy images. *Cytometry A* 58, 167-176 (2004).
- 561 9 Han, Y. et al. Brownian motion of an ellipsoid. *Science* 314, 626-630 (2006).
- 562 10 Fakhri, N., MacKintosh, F. C., Lounis, B., Cognet, L. & Pasquali, M. Brownian motion
563 of stiff filaments in a crowded environment. *Science* 330, 1804-1807 (2010).
- 564 11 Schutz, G. J., Schindler, H. & Schmidt, T. Single-molecule microscopy on model
565 membranes reveals anomalous diffusion. *Biophys. J.* 73, 1073-1080 (1997).
- 566 12 Tardin, C., Cognet, L., Bats, C., Lounis, B. & Choquet, D. Direct imaging of lateral
567 movements of AMPA receptors inside synapses. *EMBO J.* 22, 4656-4665 (2003).
- 568 13 Kusumi, A., Sako, Y. & Yamamoto, M. Confined lateral diffusion of membrane
569 receptors as studied by single particle tracking (nanovid microscopy). Effects of calcium-
570 induced differentiation in cultured epithelial cells. *Biophys. J.* 65, 2021-2040 (1993).
- 571 14 Han, Y., Alsayed, A., Nobili, M. & Yodh, A. G. Quasi-two-dimensional diffusion of
572 single ellipsoids: aspect ratio and confinement effects. *Phys Rev E Stat Nonlin Soft*
573 *Matter Phys* 80, 011403 (2009).

574
575





a**b****c**